HAL
open science

# The influence of silicon in tempered martensite: Understanding the microstructure-properties relationship in 0.5-0.6 wt.% C steels

B. Kim, Elodie Boucard, T. Sourmail, D. San Martin, Nathalie Gey, P. E. J. Rivera-Diaz-Del-Castillo

## To cite this version:

B. Kim, Elodie Boucard, T. Sourmail, D. San Martin, Nathalie Gey, et al.. The influence of silicon in tempered martensite: Understanding the microstructure-properties relationship in 0.5-0.6 wt.% C steels. Acta Materialia, 2014, 68, pp.169-178. 10.1016/j.actamat.2014.01.039 . hal-01513743

**HAL Id: hal-01513743**

**https://hal.univ-lorraine.fr/hal-01513743v1**

Submitted on 3 Dec 2020

**HAL** is a multi-disciplinary open access archive for the deposit and dissemination of scientific research documents, whether they are published or not. The documents may come from teaching and research institutions in France or abroad, or from public or private research centers.

L'archive ouverte pluridisciplinaire **HAL**, est destinée au dépôt et à la diffusion de documents scientifiques de niveau recherche, publiés ou non, émanant des établissements d'enseignement et de recherche français ou étrangers, des laboratoires publics ou privés.

# The influence of silicon in tempered martensite: Understanding the microstructure–properties relationship in 0.5–0.6 wt.% C steels

B. Kim [a,1], E. Boucard [b], T. Sourmail [c], D. San Martín [d], N. Gey [b], P.E.J. Rivera-Díaz-del-Castillo [a,*]

[a] *Department of Materials Science and Metallurgy, University of Cambridge, 27 Charles Babbage Road, Cambridge CB3 0FS, UK*
[b] *LEM3, CNRS UMR 7239, Université de Lorraine, Metz 57045, France*
[c] *ASCOmetal-CREAS (Research Centre) Metallurgy, BP 70045, 57301 Hagondange Cedex, France*
[d] *MATERALIA Group, Department of Physical Metallurgy, Centro Nacional de Investigaciones Metalúrgicas (CENIM-CSIC), Av. Gregorio del Amo 8, 28040 Madrid, Spain*

**Abstract**

The strengthening contributions in medium-carbon tempered martensite are unveiled in this work. By using transmission electron microscopy and synchrotron radiation X-ray diffraction, the different microstructural features have been captured; these include precipitation, grain boundary, solid solution and dislocation forest strengthening. The evolution of these features was observed as a function of tempering temperature and silicon content. In trying to elucidate the nature of grain boundary strengthening, three approaches are presented, including a plasticity model based on irreversible thermodynamics, misorientation angle characterization by electron backscatter diffraction, and transmission electron microscopy analysis of failed regions. Based on the findings, it is concluded that silicon inhibits martensite recovery, and that at low tempering temperatures, lath boundaries also appear to contribute to strengthening.

*Keywords:* Strengthening mechanism; Martensite; Tempering; Silicon

## 1. Introduction

Throughout martensite tempering, numerous changes occur in the microstructure that are reflected in the mechanical properties. In order to successfully model strengthening, it is crucial to understand the key microstructural parameters. Hutchinson et al. [1] gave an account of the different microstructural properties occurring in as-quenched steels with varying carbon contents. These included contributions from the grain size, forest dislocation, and the amount of carbon segregated to defect sites. Nevertheless, in the case of tempered martensite, there are further aspects that need to be considered. For instance, the hardening effects of carbide precipitation, as well as the processes of martensite recovery need to be accounted for.

Typically, the strengthening mechanisms operating in this family of steels are known to be solid solution strengthening, forest dislocation hardening, precipitate hardening and grain boundary strengthening. The last term has proven to be a challenge, owing to the complex microstructure of medium-carbon martensitic steels. Quenching from the austenite phase results in a complex microstructure, which consists of hierarchical substructures formed within prior austenite grains (PAGs), involving packets and blocks of individual laths [2].

* Corresponding author.
*E-mail address:* pejr2@cam.ac.uk (P.E.J. Rivera-Díaz-del-Castillo).
[1] Present address: Department of Materials Science and Engineering, Delft University of Technology, Mekelweg 2, 2628CD Delft, The Netherlands.

The general form of the equation typically used to describe the yield stress of lath martensite, $\sigma_y$, is the following [3]:

$$\sigma_y = \sigma_0 + \sigma_{ss} + \sigma_{pcpt} + \sigma_\rho + k_{HP} d^{-\frac{1}{2}}, \quad (1)$$

where $\sigma_0$ is the lattice friction stress for pure Fe, $\sigma_{ss}$ is the solid solution strengthening term, $\sigma_{pcpt}$ is the strength increment due to precipitation hardening, $\sigma_\rho$ is the forest dislocation hardening term due to the presence of dislocations in lath boundaries and sub-block boundaries, and $k_{HP} d^{-\frac{1}{2}}$ is the grain boundary strengthening based on the Hall–Petch effect.

The widely accepted Hall–Petch relationship states that strength is inversely proportional to the square root of the grain size. However, the question remains: what acts as the "effective" grain size? For instance, for lath martensite containing 0.4 wt.% C, Daigne et al. [4] showed that the grain boundary effect was determined by either the lath width or the packet size, depending on the form of carbides present. For an Fe–23Ni martensitic steel, Shibata et al. showed a strength increment due to the presence of block boundaries [5]. The fundamental concept is based on the fact that dislocations interact with the boundaries. Therefore, for the time being, the Hall–Petch term in Eq. (1) is replaced by a broader term: sub-grain boundary strengthening, $\sigma_{sg}$.

The first part of this work presents experiments carried out to determine the individual strengthening contributions in Eq. (1). The second part presents the plasticity model and supporting experimental work using electron backscatter diffraction (EBSD) and transmission electron microscopy (TEM), with the aim of developing an understanding of the key microstructural parameters which define the tensile properties of tempered martensite, particularly addressing the changes taking place throughout tempering under the effect of silicon.

## 2. Alloys and treatments

Three alloys containing different Si contents have been cast, processed and studied (Table 1). The notation used throughout is HS, MS and LS for the high (2.3 wt.%), medium (1.7 wt.%) and low (1.4 wt.%) Si content alloy, respectively.

Details of the casting process have been reported in a previous work by the authors [6].

## 3. Strengthening contributions

### 3.1. Tensile testing

For each grade, blanks of approximately $10 \times 10 \times 100\ \text{mm}^3$ were cut from a previously forged bar at mid-radius. The blanks were austenitized for 15 min (holding time) at 880 °C in a salt bath to minimise decarburization, quenched in oil and allowed to reach room temperature. They were subsequently tempered for 30 min at either 250, 350 or 450 °C in a laboratory furnace, ensuring that no more than 1 h was left between quenching and tempering, as previous results had suggested a possible influence of the duration of the interruption [7]. The sample notation used throughout consists of the alloy followed by the tempering temperature, e.g. HS-250 refers to the HS alloy tempered at 250 °C.

Tensile specimens (6 mm gauge diameter) were machined from the heat-treated blanks and tested in accordance with ISO 6892-1 on a Zwick RKM200 machine. Each condition was tested twice and all samples failed by necking. Tensile curves for HS alloy are shown in Fig. 1. The yield stress ($\sigma_{y,0.2}$), the ultimate tensile stress ($\sigma_{UTS}$), the elongation ($A$) and the reduction area ($Z$) for all conditions are summarized in Table 2.

Having determined $\sigma_y$ from tensile testing, if the terms $\sigma_0, \sigma_\rho, \sigma_{pcpt}, \sigma_{ss}$ can be experimentally determined, then, by subtraction, the unaccounted strength can be attributed to the sub-grain boundary strengthening ($\sigma_{sg}$) term.

### 3.2. Solid solution strengthening, $\sigma_{ss}$

Empirical data [8] have been used in order to estimate the degree of solid solution strengthening based on alloy composition, Table 3, where $\Delta\sigma/\text{X}i$ wt.% is the strength increment per 1 wt.% of $i$, and $i$ wt.% is the weight percentage of $i$ solute. The overall $\sigma_{ss}$ term is given by the sum of all $\Delta\sigma_{ss,i}$ terms, where the latter is given by the product of the $\Delta\sigma/i$ wt.% and $i$ wt.% terms.

The effect of carbon in solid solution has been neglected for the time being, under the assumption that most carbon would have precipitated during tempering. The strength increment owing to solid solution only contributes marginally to the total strength of the alloy. Attention is drawn to chromium. In the literature, its effect in solid solution is still not clear, as contradictory strengthening effects have been ascribed to it [9,10]. Kelley and Stoloff [10] have concluded that between 147 and 300 K, up to 10 wt.% Cr in high-purity iron has little effect on the yield strength, given the small atomic misfit between Cr and Fe, and their equal (body-centred cubic) crystal structure. Therefore the effect of Cr as a solid solution strengthener has been omitted.

### 3.3. Precipitation hardening, $\sigma_{pcpt}$

Microstructural characterization of the intralath carbides was carried out using TEM (Philips CM30). The

Table 1
Measured chemical composition of alloys, in wt.%, balance Fe.

| | C | Si | Mn | Cr | Mo | V | Ti | Ni | Cu | S | P |
|---|---|---|---|---|---|---|---|---|---|---|---|
| HS | 0.56 | 2.30 | 0.69 | 0.89 | 0.02 | 0.10 | 0.03 | 0.20 | 0.15 | 0.02 | 0.01 |
| MS | 0.55 | 1.71 | 0.71 | 0.89 | 0.02 | 0.10 | 0.03 | 0.20 | 0.16 | 0.03 | 0.01 |
| LS | 0.55 | 1.43 | 0.72 | 0.91 | 0.02 | 0.10 | 0.03 | 0.21 | 0.16 | 0.02 | 0.01 |

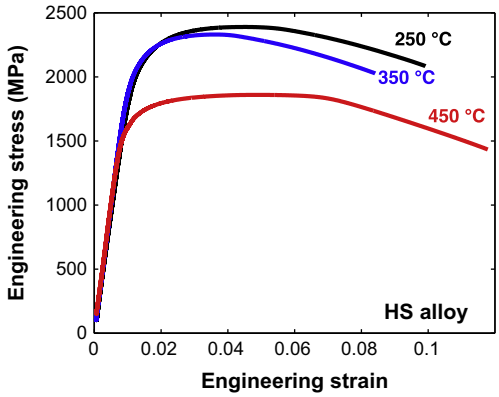


Fig. 1. Stress–strain curves for HS.

Table 2
Summary of tensile properties.

| Condition | $\sigma_{y,0.2}$ (MPa) | $\sigma_{UTS}$ (MPa) | $A$ (%) | $Z$ (%) |
|---|---|---|---|---|
| HS-250 | $2038 \pm 2$ | $2382 \pm 11$ | 8.8 | 33 |
| HS-350 | $2039 \pm 1$ | $2324 \pm 10$ | 6.5 | 22 |
| HS-450 | $1602 \pm 8$ | $1866 \pm 8$ | 9.2 | 39.8 |
| MS-250 | $1991 \pm 0.2$ | $2311 \pm 7$ | 2.3 | 16.1 |
| MS-350 | $1972 \pm 3$ | $2233 \pm 6$ | 2 | 38.4 |
| MS-450 | $1550 \pm 4$ | $1727 \pm 5$ | 3.7 | 34.5 |
| LS-250 | $1936 \pm 52$ | $2275 \pm 17$ | 2.7 | 38.0 |
| LS-350 | $1916 \pm 3$ | $2187 \pm 0.2$ | 1.6 | 19.6 |
| LS-450 | $1511 \pm 7$ | $1672 \pm 10$ | 3.6 | 35.8 |

Table 3
Estimating solid solution strengthening contribution (units in MPa).

| Element | Si | Mn | Cr | Cu | Ni | **HS** | **MS** | **LS** |
|---|---|---|---|---|---|---|---|---|
| $\Delta\sigma/i$ wt.% | 83 | 32 | −31 | 39 | 0 | **219** | **171** | **148** |

procedure is described in Ref. [7]. The heat treatments were performed in an Adamel Lhomargy dilatometer (DT1000). The specimens were cylindrical rods 3 mm in diameter and 12 mm long. The same heat treatment was applied as in Section 3.1, with additional tempering conditions at 300 and 400 °C. Bright-field images are shown in Fig. 2, where a summary of the microstructural analysis is also presented.

The microstructure of a couple of tensile specimens was also analysed using TEM, where regions exhibiting little deformation were selected. The carbide distribution was very similar to the one obtained from dilatometry specimens, thus justifying the use of the carbide distribution obtained from dilatometry specimens for the tensile properties that were heat treated by oil-quenching and furnace-tempering. In estimating $\Delta\sigma_{pcpt}$, particle by-passing is assumed, and approximated by employing the Ashby–Orowan equation [11]:

$$\Delta\sigma_{pcpt} = \left(\frac{0.538Gb\sqrt{V_f}}{X}\right)\ln\left(\frac{X}{2b}\right), \tag{2}$$

where $G$ is the shear modulus, $b$ is the Burgers vector, $V_f$ is the volume fraction, and $X$ is the diameter of the particle in mm, taken to be the equivalent spherical diameter of the rod-shaped intralath carbides.

Previous X-ray diffraction (XRD) analysis showed that the ferrite lattice parameters for HS and LS are $a = 2.8550$ and 2.8666 Å, respectively [6]. Considering the $\frac{1}{2}a\langle 1\,1\,1\rangle$ Burgers vector in ferrite, the corresponding $b$ value, determined by $\frac{\sqrt{3}}{2}a$, are 2.473 and 2.483 Å, for HS and LS, respectively. $b$ for MS is interpolated to be 2.480 Å.

In the case of the shear modulus, Ghosh and Olson reported that for a lath microstructure the high dislocation density decreases the shear modulus by ~5% compared to the cubic ferrite counterpart, thus $G_{\text{ferrite}} = 80$ GPa corresponds to $G_{\text{lath}} = 76$ GPa [12].

The volume fraction was estimated based on carbide size and spacing. The 0.08 value used in this work agrees with the expected cementite fraction 0.083 obtained from ThermoCalc. However, all three alloys when tempered at 450 °C showed a significantly reduced amount of intralath carbides, as shown in Fig. 2. In order to account for this apparent lower volume fraction of intralath carbides, a value of 0.05 was used for 450 °C.

Using Eq. (2), Table 4 summarizes values for $X$, $V_f$, and the corresponding $\sigma_{pcpt}$ values. Given the absence of data for the 450 °C condition, $r_{equiv}$ values for 400 °C are used, and instead a lower volume fraction is assigned.

The values obtained for $\Delta\sigma_{pcpt}$ appear to contribute approximately one-third of the total yield stress. Therefore, the other terms also need to be quantified.

### 3.4. Dislocation forest hardening, $\sigma_\rho$

The hardening contribution from dislocations can be estimated from:

$$\Delta\sigma_\rho = M\alpha Gb\sqrt{\rho}, \tag{3}$$

where $M$ is the Taylor factor, taken to be 3 [13], $\alpha = 0.25$ [13], and $\rho$ is the dislocation density following heat treatment.

Alloys HS and LS were characterized using high-energy X-rays from a synchrotron source [6]. The samples were first heat treated in the dilatometer as described in Section 3.3, and then measured in the synchrotron facility at room temperature. Based on the line-broadening method [14], the dislocation density was estimated from the microstrains, $\varepsilon_{micro}$. Rietveld refinement was performed using MAUD software [15]. It is worth noting that the instrumental broadening contribution coming from the instrument used (beamline I11 at Diamond Light Source) is assumed to be negligible [16]. Christien et al. derived an expression for the dislocation density [17]:

$$\rho = \frac{3E}{Gb^2(1+2\nu^2)}\varepsilon_{micro}^2, \tag{4}$$

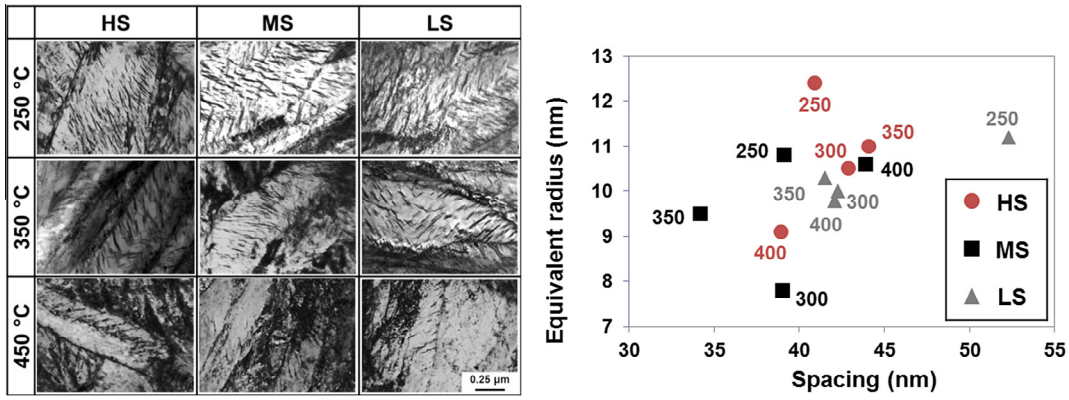


Fig. 2. Representative bright-field images showing intralath carbide precipitates, and summary of carbide size and spacing for all conditions, from dilatometry specimens.

Table 4
Estimating precipitation hardening, $X = 2 \times r_{equiv}$.

| Condition | $X$ (nm) | $V_f$ | $\Delta\sigma_{pcpt}$ (MPa) |
|---|---|---|---|
| HS-250 | 15.8 | 0.08 | 628 |
| HS-350 | 14.0 | 0.08 | 683 |
| HS-450 | 14.3 | 0.05 | 540 |
| MS-250 | 13.8 | 0.08 | 693 |
| MS-350 | 12.1 | 0.08 | 757 |
| MS-450 | 13.5 | 0.05 | 555 |
| LS-250 | 14.3 | 0.08 | 676 |
| LS-350 | 13.1 | 0.08 | 717 |
| LS-450 | 12.5 | 0.05 | 587 |

where $E$ is the Young's modulus and $\nu$ is the Poisson's ratio. Eq. (4) is employed in this work.

During the synchrotron measurements, only alloys HS and LS were characterized. The dislocation density for MS is interpolated from the previous two values. Table 5 provides a summary of $\rho$ and $\Delta\sigma_\rho$. The order of magnitude $\sim 10^{15}$ m$^{-2}$ corresponds to the typically reported value for martensitic steels [17,18].

Throughout tempering, as a consequence of the martensite recovery process, the dislocation density decreases. Thus a decrease in the $\sigma_\rho$ contribution is also observed for samples tempered at higher temperatures.

Table 5
Estimating forest dislocation hardening.

| Condition | $\rho \times 10^{15}$ m$^{-2}$ | $\Delta\sigma_\rho$ (MPa) |
|---|---|---|
| HS-250 | 7.1 | 1184 |
| HS-350 | 4.4 | 939 |
| HS-450 | 3.8 | 866 |
| MS-250 | 6.8[a] | 1161 |
| MS-350 | 3.9[a] | 885 |
| MS-450 | 2.2[a] | 682 |
| LS-250 | 6.6 | 1150 |
| LS-350 | 3.7 | 856 |
| LS-450 | 1.6 | 568 |

[a] Indicates value interpolated from HS and LS.

## 4. Estimating the grain size effect

Substituting the numerical values into (1), the grain size effect contribution can be worked out by subtraction, as summarized in Table 6 under column '$\sigma_{sg}$ in (1)'. The values within brackets for $\sigma_{sg}$ represent negative values. Given that it has no physical meaning to have a negative stress contribution in this case, an alternative $\sigma_y$ expression is sought. Often, in plasticity modelling, the flow stress is given by [19]:

$$\tau = \tau_0 + \tau_{ss} + \tau_b + \sqrt{\tau_{in}^2 + \tau_{pcpt}^2}, \tag{5}$$

where $\tau$ is the shear stress, and the subscripts 0, $ss$, $b$, $in$ and $pcpt$ refer to the shear stress of pure Fe, solid solution, kinematic hardening, isotropic hardening and precipitate hardening, respectively. The kinematic and isotropic terms will be explored further on. Using the same principle as in Eq. (5), a modified expression for $\sigma_y$ is proposed:

$$\sigma_y = \sigma_0 + \sigma_{ss} + \sigma_{sg} + \sqrt{\sigma_\rho^2 + \sigma_{pcpt}^2}, \tag{6}$$

The expression in Eq. (1) might overestimate the dislocation forest and precipitation hardening terms. This is consistent with the observations made by Queyreau et al. [20], where they have evaluated both the individual and the superimposed contribution of these two mechanisms

Table 6
Unaccounted stress: grain size effect (MPa).

| Condition | $\sigma_y$ | $\sigma_0$ | $\sigma_{pcpt}$ | $\sigma_{ss}$ | $\sigma_\rho$ | $\sigma_{sg}$ in (1) | $\sigma_{sg}$ in (6) |
|---|---|---|---|---|---|---|---|
| HS-250 | 2038 ± 2 | 54 | 628 | 219 | 1184 | (46) | 425 |
| HS-350 | 2039 ± 1 | 54 | 683 | 219 | 939 | 144 | 604 |
| HS-450 | 1602 ± 8 | 54 | 540 | 219 | 866 | (77) | 309 |
| MS-250 | 1991 ± 0.2 | 54 | 693 | 169 | 1161 | (88) | 414 |
| MS-350 | 1972 ± 3 | 54 | 757 | 169 | 885 | 105 | 582 |
| MS-450 | 1550 ± 4 | 54 | 555 | 169 | 682 | 88 | 446 |
| LS-250 | 1936 ± 52 | 54 | 676 | 144 | 1150 | (92) | 400 |
| LS-350 | 1916 ± 3 | 54 | 717 | 144 | 856 | 141 | 597 |
| LS-450 | 1511 ± 7 | 54 | 587 | 144 | 568 | 155 | 493 |

using the quadratic mixture law. Applying Eq. (6), a new set of $\sigma_{sg}$ values is obtained, shown in Table 6, under the column '$\sigma_{sg}$ in (6)'.

There is an apparent increase in $\sigma_{sg}$ as the tempering temperature goes from 250 to 350 °C, followed by a decline between 350 and 450 °C. An examination of the microstructure is performed in order to understand the observed trends.

**Prior austenite grain size**

The PAG size was revealed by the method of thermal etching [21]. The mean PAG size was found to be 11.4 ± 1.1 and 12.3 ± 1.1 μm for MS and LS, respectively. The PAG boundaries could not be revealed for the HS alloy.

**Lath width**

In trying to determine the hypothetical role that individual laths play during yielding in lath martensite, a similar microstructural analysis as the one carried out for intralath carbides was performed to measure lath width. Twenty-five measurements were taken from two TEM frames. The averages are tabulated in Table 7, where stereological corrections have been applied [22]. Based on the TEM characterization, it appears that the lath width increase with tempering temperature is arrested for the highest Si content, HS. In the case of the LS alloy, the increase is 2-fold.

Fig. 3 shows a plot of the estimated $\sigma_{sg}$ contribution vs. lath width. For illustrative purposes, two values of $k_{HP}$ have been considered to show the predicted Hall–Petch effect. Most of the 350 and 450 °C data points correspond to $k_{HP}$= 0.19 MPa m$^{-1/2}$, which is in agreement with the values 0.21 and 0.20 MPa m$^{-1/2}$ reported by Shibata et al. for block boundaries [5], and Wang et al. [23] for martensite packets, respectively. On the other hand, the 250 °C conditions, as well as HS-450, appear to correspond to a lower value of $k_{HP}$ = 0.12 MPa m$^{-1/2}$.

Takeda et al. [24] showed that $k_{HP}$ varied as a function of carbon content in solid solution, where values ranged between 0.12 and 0.6 MPa m$^{-1/2}$, corresponding to 4–60 ppm C. The lower $k_{HP}$ observed for the 250 °C conditions would therefore imply a lower carbon content in solid solution. Nevertheless, there might be additional factors influencing the value of $k_{HP}$ other than carbon content, such as the nature of the boundaries present. This also raises a question as to whether lath units also contribute to strengthening, in spite of their low misorientation angles. The "effective" grain size is investigated by using two additional methods: plasticity modelling and EBSD.

Table 7
Lath width (in nm) as a function of temperature and Si content.

| | 250 °C | 350 °C | 450 °C |
|---|---|---|---|
| HS | 91 ± 25 | 96 ± 28 | 122 ± 41 |
| MS | 94 ± 23 | 89 ± 28 | 154 ± 46 |
| LS | 74 ± 16 | 105 ± 29 | 154 ± 63 |

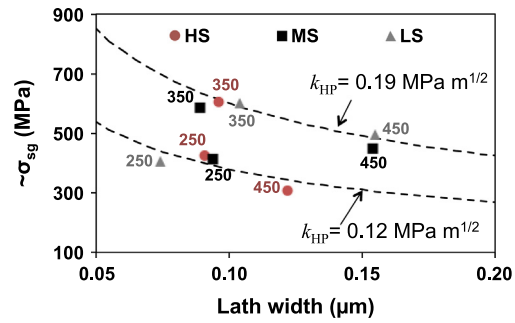


Fig. 3. Plot of estimated $\sigma_{sg}$ contribution vs. lath width, with fitted $k_{HP}$ values.

### 4.1. Modelling plasticity

In this work, the plasticity model based on irreversible thermodynamics developed by Huang et al. for ultrafine grains [13] is applied for lath martensite—see their original work for details of this model. Previously, it was defined that the flow stress of the alloy can be expressed in terms of additive terms, as shown in Eq. (5). The two concepts to introduce next are the kinematic and isotropic hardening terms.

#### 4.1.1. Kinematic hardening

During plastic deformation, a grain will experience piling-up of dislocations at the boundary, as shown in Fig. 4. This micrograph comes from the region failed by necking for sample HS-250, using a F20 Tecnai FEG-TEM in scanning–transmission mode. The light region represents an individual lath, where piled-up dislocations are clearly visible at the lath boundary. For a grain size $D$, the number of dislocations piling-up, $n$, is bound to change as follows:

$$\tau_b = \frac{Gb}{D} n, \tag{7}$$

The evolution of $n$ with respect to the applied plastic shear strain, $\gamma$, is given by:

$$\frac{dn}{d\gamma} = \frac{\lambda}{b}\left(1 - \frac{n}{n^*}\right), \tag{8}$$

where $\lambda$ is the mean spacing between slip planes at the grain boundaries, and $n^*$ is the maximum number of dislocations that can pile-up at the grain boundary on a given slip plane. Beyond this number, the accumulated stress is large enough for the dislocation to penetrate through the grain boundary, or for climb or cross-slip to occur [13].

By combining Eq. (7) and integrating (8), and assuming that $n = 0$ when $\gamma_p = 0$, the kinematic hardening term becomes:

$$\tau_b = \frac{Gb}{D} n^* \left[1 - \exp\left(-\frac{\lambda}{bn^*}\gamma\right)\right], \tag{9}$$

The use of the correct $n^*$ value is crucial. In interstitial-free steels, this value was observed to be between 3 and 4 [13],

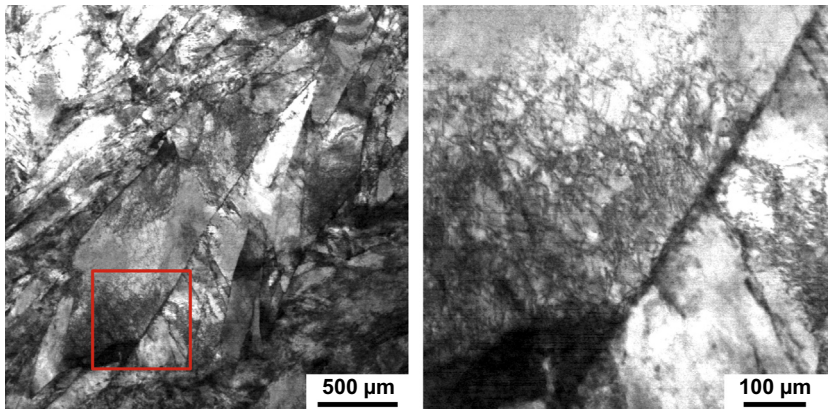


Fig. 4. HRTEM images showing piled-up dislocations at lath boundaries of HS-250 failed by necking.

although in precipitation-hardened Al steels this value was found to be 9 and 60 for 7xxx and 6xxx alloys, respectively [25,26].

*4.1.2. Isotropic hardening*

This hardening contribution is due to the dislocations in the grain interior, equivalent to the previously defined $\sigma_\rho$ term [27,13]:

$$\tau_{in} = \alpha G b \sqrt{\rho_{initial}}, \tag{10}$$

During plastic deformation, the following cases must be considered regarding dislocations: generation, glide along slip systems and annihilation. The model developed by Huang et al. [13], based on irreversible thermodynamics and consistent with the Kocks–Mecking approach, showed that the dislocation density varied with shear strain:

$$\frac{d\rho}{d\gamma} = k_1\sqrt{\rho} - k_2\rho, \tag{11}$$

where $k_1$ is the storage coefficient and $k_2$ is the dynamic recovery coefficient.

Rivera-Díaz-del-Castillo et al. [19] derived an expression for the dislocation density evolution during plastic deformation, which incorporated the dislocation forest and precipitation hardening terms:

$$\frac{d\rho}{d\gamma_p} = \frac{1}{1+\left(\frac{\tau}{Gb\sqrt{\rho}}\right)-\frac{1}{2}C\alpha_c}\left[\frac{\sqrt{\tau_{in}^2+\tau_p^2}}{Gb^2} - \left(1+\frac{\tau_b}{Gb\sqrt{\rho}}\right)\frac{v_0}{\dot{\gamma}_p}\exp\left(-\frac{\Delta G}{k_B T}\right)\right]\rho, \tag{12}$$

where $C = -100$ and $\alpha_c = 0.25$ are material constants which were taken from the literature, and $\Delta G$ is the effective activation energy accounting for the average of the activation energies for dislocation climb or cross-slip, which was taken to be 0.766 eV [13]. $k_B$ and $T$ are the Boltzmann constant and the absolute temperature, respectively, and the shear strain rate $\dot{\gamma} = 0.002\ \mathrm{s}^{-1}$.

As the original model by Huang et al. is only concerned with the plastic behaviour of steels, it was necessary to modify the kinematic strengthening term in (9). The reason being that at the beginning of the plastic deformation, i.e. when $\gamma_p = 0$, this would give $\tau_b = 0$. However, from the yielding point there is already some contribution from the grain size ($\sigma_{sg}$). Therefore, in order to carry this term forward, the following is proposed:

$$\tau_b = \tau_{b,0} + \frac{Gb}{D}n^*\left[1 - \exp\left(-\frac{\lambda}{bn^*}\gamma\right)\right], \tag{13}$$

where $\tau_{b,0}$ would be the equivalent shear stress for the $\sigma_{sg}$ obtained previously, and has been treated as a constant.

*4.2. Parametric analysis*

It is a well-established concept that the onset of necking occurs when the following condition—known as Considère's criterion—is achieved:

$$\sigma = \frac{d\sigma}{d\epsilon}. \tag{14}$$

All the parameters that were obtained experimentally have been used as input to the model. By adjusting $D$ and $n^*$ while keeping all the other parameters constant, the values were refined until the best agreement is obtained between the model and the stress–strain experimental data. During plastic deformation, as dislocations are generated from sources within grains, the number of dislocation pile-ups is given by [28]:

$$n = \frac{L\tau}{A}, \tag{15}$$

where $L$ is the distance between the source and the boundary, $A$ is $\frac{Gb}{\pi}$ or $\frac{Gb}{\pi(1-\nu)}$ for screw and edge dislocations, respectively. If the assumption is made that the dislocation generation source is located in the middle of the grain, then it might be possible to state that for a bigger grain size, i.e. a larger $L$ value, the higher the $n$ becomes. In other words, larger grains might be able to retain more dislocations, increasing the value of $n^*$. Therefore, it appears that $n^*$ increases with increasing $D$. The final values of $D$ and $n^*$ are summarized in Fig. 5.

The fitted values of $D$ are 1, 1.5, 1 and 2 μm for the conditions HS-250, HS-450, LS-250 and LS-450, respectively.

The grain size increase with temperature is likely to be due to the recovery of the martensite, which is thought to take place near 400 °C [29]. The increase in $D$ between 250 and 450 °C, would explain the apparent decrease in $\sigma_{sg}$ observed in Fig. 3. The second approach to estimate $D$ is by using EBSD, and is presented in the following section.

### 4.3. EBSD

The conditions analysed by EBSD were: HS-250, HS-450, LS-250 and LS-450. These samples were heat treated in laboratory furnaces, austenitized at 880 °C, quenched in ice brine and tempered for 1800 s. Samples were prepared to an OPS colloidal silica finish.

The EBSD patterns were acquired on a high-resolution Quantax Bruker EBSD camera attached to a Zeiss Supra 40 field emission gun scanning electron microscope. All measurements were done at an accelerating voltage of 20 kV. The step size used varied between 50 and 75 nm. Post-processing of the data was carried out in Tango (HKL Channel 5). A histogram plot of the misorientation angle, $\theta_{mis}$, produced by the software is shown in Fig. 6 for all conditions. The results follow the same trend as those reported by Hutchinson et al., where most of the angles are in the range of 5–15°, and in the range of $\theta_{mis} > 45°$. The peaks in the region of 54–60°are characteristic of certain orientation relationships between austenite and martensite, such as Nishiyama–Wassermann and Kurdjumov–Sachs [1,2].

It is worth noting that HS-250 and HS-450 overlap at all angles. When comparing HS-250 and LS-250, the main difference is observed in the range of $10 < \theta_{mis} < 20°$. The change in the misorientation angle distribution with temperature in LS is more significant than in HS. Thus, it appears that recovery is affected by the presence of Si. This will be explored further in Section 5.

The image quality (IQ), or band contrast (BC), maps are shown in Fig. 7 (top row), where the initial index rate during acquisition is shown for each sample. The images shown on the inverse pole figure (IPF) maps (bottom row) have been corrected for noise reduction, where, iteratively, the index rate was artificially increased to ~100%. Note that when noise reduction is applied, the grains appear to become bigger. However, this is an artificial effect, as the non-indexed regions are assigned a crystallographic orientation based on their neighbours. This complicates grain size measurements due to the fact that the results are highly dependent on data post-processing. Therefore two sets of measurements have been taken: one using the original image, and another where the index rate was increased to ~100%. Thus, the former would represent the lower boundary, whereas the latter shows the upper boundary. The actual grain size is likely to be within this range.

#### 4.3.1. Grain size determination based on misorientation angle

Generally, high-angle boundaries are considered to arrest dislocation motion, while, on the other hand,

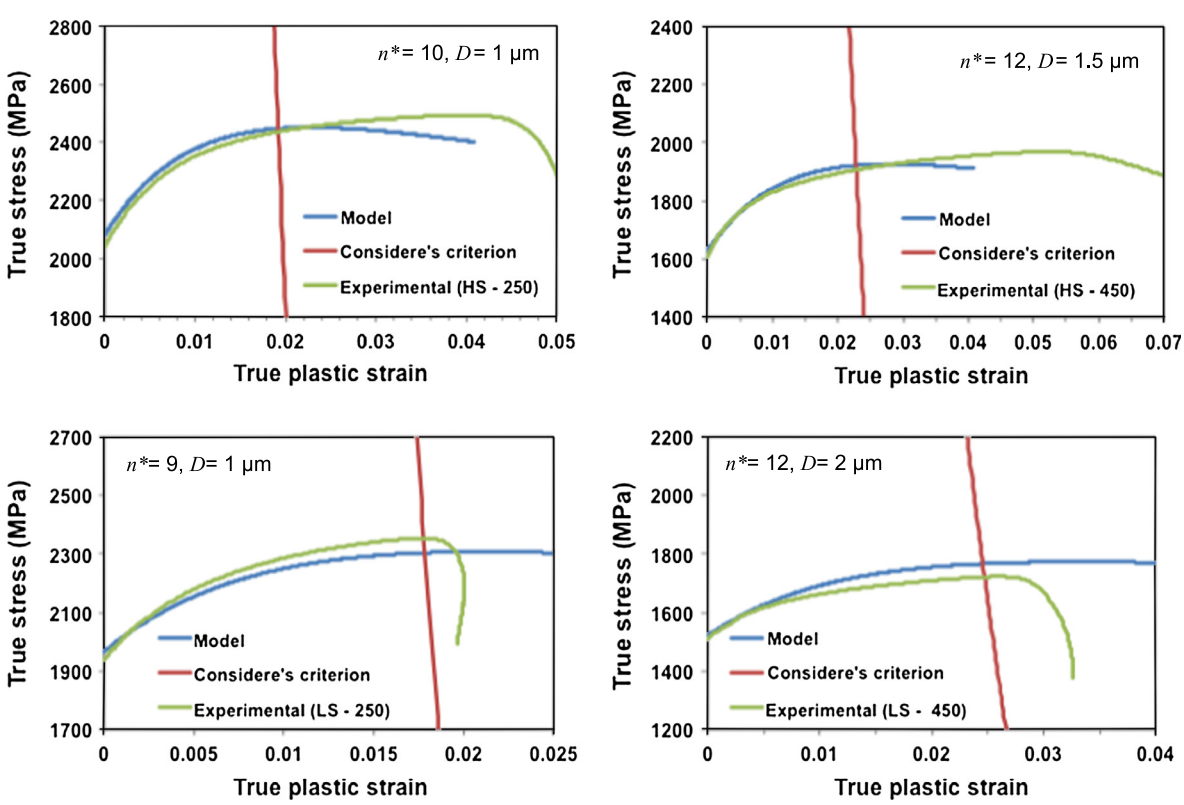


Fig. 5. Plasticity modelling for HS and LS alloys.

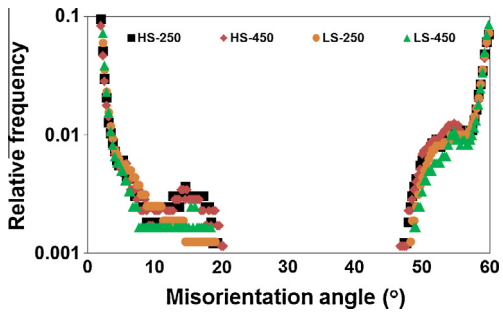


Fig. 6. Histogram plotting frequency of misorientation angle.

low-angle boundaries would be transparent to dislocations. It is reported in the literature that the transition between low- and high-angle boundaries is in the region of 10–20°. $\theta_{mis} = 15°$ is taken to be the critical misorientation angle [30,31]. The black lines on the IPF maps in Fig. 7 represent those boundaries where $\theta_{mis} > 15°$.

The grain area method was used, where by defining the critical grain boundary as 15°, the number of grains was detected. The equivalent spherical diameter is summarized in Table 8. The values obtained by EBSD are slightly lower than those obtained by plasticity modelling.

Morito et al. showed that lath boundaries have a misorientation angle of 2.8–2.9°, and that in general low-angle boundaries are transparent to dislocation movement. However, some researchers have reported a direct strengthening contribution from individual laths [32,4]. Furthermore, Fig. 4 shows tangled dislocations at the lath boundary. Therefore, it is possible that at low tempering temperatures, where the initial dislocation density is still high, individual laths can contribute to strengthening.

Table 8
Comparing grain size values (units in μm).

| | HS-250 | HS-450 | LS-250 | HS-450 |
|---|---|---|---|---|
| Plasticity model | 1 | 1.5 | 1 | 2 |
| EBSD | 0.4–0.6 | 0.4–0.6 | 0.4–0.6 | 0.4–0.7 |

The question raised at this point is whether there is a single microstructural unit that acts as the effective grain size. It appears that it would be more appropriate to express grain boundary strengthening as an additive term. Although the nature of lath boundaries might be of a low misorientation angle, the very high initial dislocation density as well as the large number of lath boundaries would contribute significantly to strengthening.

## 5. The effect of silicon on martensite recovery

Using the same sample preparation procedure as in Section 4.3, a few heat treatments were designed to study the effect of Si on martensite recovery by XRD methods. Flat-plate specimens consisting of a surface area of $20 \times 20\ mm^2$, and a thickness of ~1 mm were prepared to an OPS colloidal silica finish. A Phillips X'Pert PW3020 diffractometer equipped with a Cu radiation source ($\lambda_{Cu} \approx 1.540598$ Å) was used. Scans were taken between $2\vartheta$ angles of 40°and 105°, using a step size of 0.035°and a dwell time of 5 s.

Fig. 8 shows the (1 1 0) and (2 1 1) ferrite peaks for alloys HS and LS. The heat treatments shown are tempered at 300 °C for 1800 and 3600 s, at 350 °C for 1800 and 3600 s, and at 400 °C for 1800 s.

The first observation that can be made is that, throughout tempering, peak sharpening occurs. This sharpening

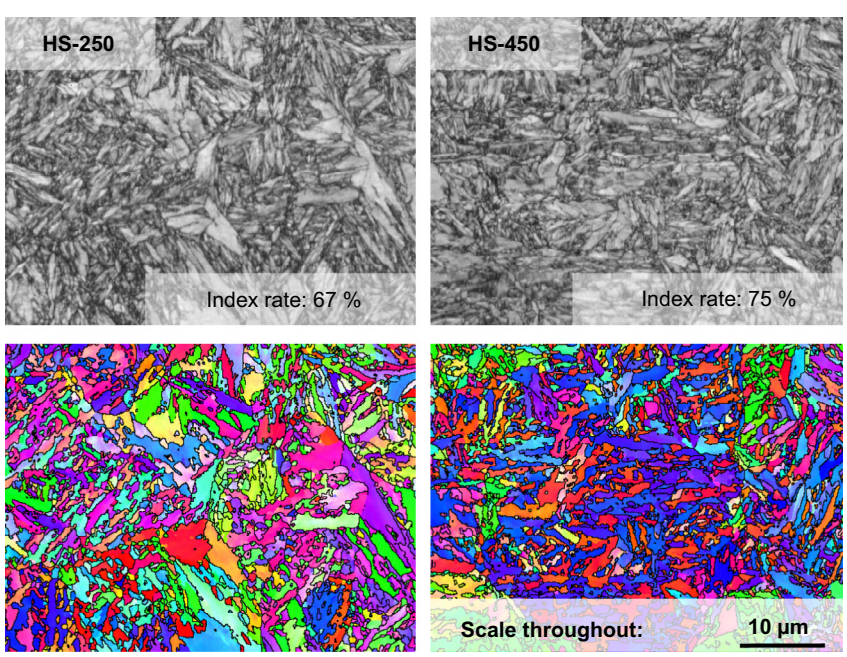


Fig. 7. IQ (top row) and IPF (bottom row) images after iterative noise reduction for samples HS-250 and HS-450.

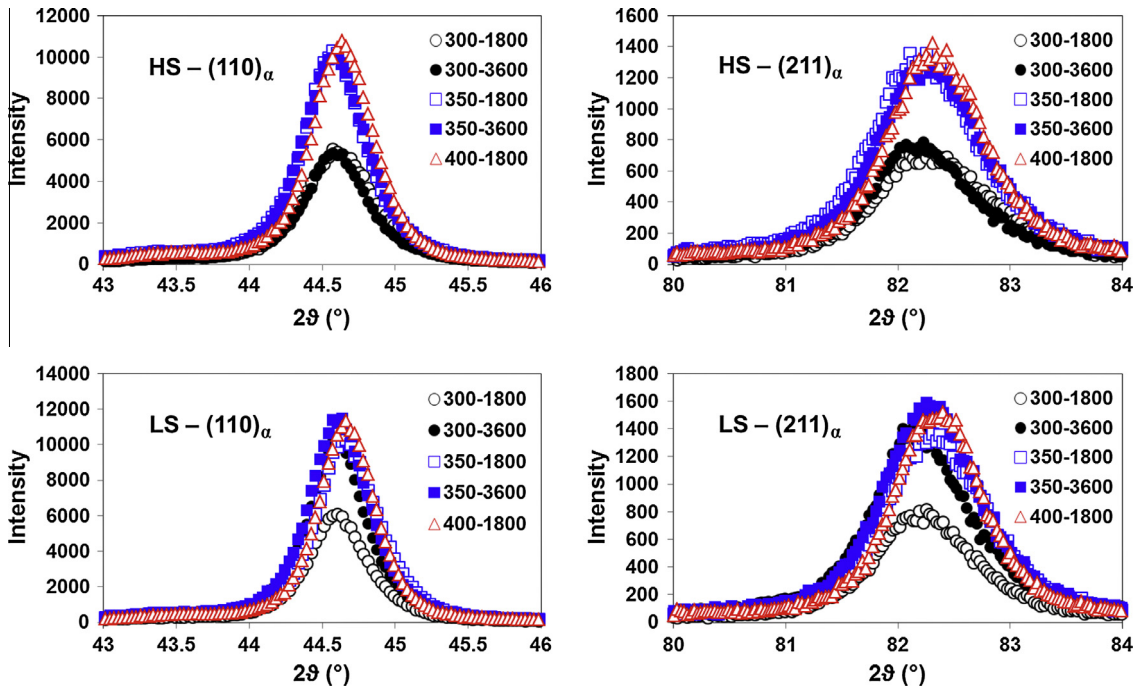


Fig. 8. Diffraction spectra for the (1 0 0) and (2 1 1) ferrite peaks. The legend summarizes the heat-treatment combinations investigated, e.g. 300–1800 stands for tempered at 300 °C for 1800 s.

occurs between 300 and 350 °C for both HS and LS alloys. Nevertheless, based on peak-broadening effects, whereas in Section 3.4, the broadening was related to the dislocation density, it is observed that in the case of LS, 3600 s tempering at 300 °C already has the same effect as 1800 s tempering at 350 °C for HS. Thus, based on these findings, the kinetics of martensite recovery appears to be influenced by Si content. At this stage, it is not possible to know whether it is a specific property of Si to delay martensite recovery, or if it is merely due to a solid solution effect in general. Nevertheless, Wittig and Frommeyer [33] reported that the presence of Si in the body-centred cubic Fe lattice caused a reduction in dislocation cross-slip with increasing Si content. When alloyed with Si, additional to the Peierls stress from the ferrite lattice, there is a stress increment in moving a dislocation, owing to an increase in the free energy due to the Si–Si interaction. Hence, dislocation cross-slip will be lower in HS than in LS, causing lower recovery kinetics with increasing Si content.

## 6. Conclusions

Owing to the complex microstructure of martensite, modelling mechanical properties is challenging. In order to understand the key microstructural features that determine plasticity, the different terms contributing to martensite tempering were identified.

1. Although precipitation hardening plays an important role, plasticity is primarily dominated by the kinematic and isotropic hardening terms.
2. In modelling the flow stress in tempered martensite, the quadratic mixture law applies for precipitation and forest dislocation hardening contributions.
3. With the necessary adjustments, a plasticity model based on ultrafine-grained steels was fitted to the experimental tensile curves. The "effective" grain size was found to be of the order of ~1 μm.
4. EBSD was used in order to reconstruct the boundaries within tempered martensite. By using the boundary condition $\theta_{mis} > 15°$, the equivalent diameter of grains was determined to be in the range of 0.4–0.7 μm.
5. Throughout martensite tempering, a decrease in dislocation density was observed. The rate of decrease was faster in the LS than in HS. It is proposed that Si plays an inhibiting role in martensite recovery.

Although some progress has been made in understanding the effect of grain size in medium-carbon tempered martensite, more research is needed to understand the microstructural changes occurring in the martensite matrix during recovery.

## Acknowledgements

B.K. and P.E.J.R. are grateful to Prof. A.L. Greer for the provision of laboratory facilities and would like to acknowledge ASCOmetal for financial support. D.S.M. would like to acknowledge the financial support from the Ministerio de Economía y Competitividad (Project No. MAT2010-19522). The authors would also like to thank the Diamond Light Source for access to Beamline I11,

and the beamline team, especially Prof. Chiu Tang and Dr. Paul Adamson, for their assistance throughout beamtime. The authors are grateful for the synchrotron sample machining by Mr. Javier Vara (CENIM).

## References

[1] Hutchinson B, Hagström J, Karlsson O, Lindell D, Tornberg M, Lindberg F, et al. Acta Mater 2011;59:5845–58.
[2] Morito S, Tanaka H, Konishi R, Furuhara T, Maki T. Acta Mater 2003;51:1789–99.
[3] Morito S, Yoshida H, Maki T, Huang X. Mater Sci Eng A 2006;438–440:237–40.
[4] Daigne J, Guttmann M, Naylor JP. Mater Sci Eng 1982;56:1–10.
[5] Shibata A, Nagashi T, Sone M, Morito S, Higo Y. Mater Sci Eng A 2010;527:7538–44.
[6] Kim B, Celada C, Sourmail T, San Martín D, Rivera-Díaz-del-Castillo PEJ. Acta Mater 2013;61:6883–992.
[7] Kim B, Celada C, San Martín D, Chao J, Vara J, Rivera-Díaz-del-Castillo PEJ. Scr Mater 2013;68:945–8.
[8] Gladman T. The physical metallurgy of microalloyed steels. London: Institute of Materials; 1997.
[9] Funakawa Y, Ujiro T. Iron Steel Inst Jpn Int 2010;50:1488–95.
[10] Kelley MJ, Stoloff NS. Metall Trans A 1976;7:331–3.
[11] Gladman T. Mater Sci Technol 1999;15:30–6.
[12] Ghosh G, Olson GB. Acta Mater 2002;50:2655–75.
[13] Huang M, Rivera-Díaz-del-Castillo PEJ, Bouaziz O, van der Zwaag S. Mater Sci Technol 2009;25:833–9.
[14] Hall WH, Williamson GK. Proc Phys Soc B 1951;64:946–53.
[15] Lutterotti L, Matthies S, Wenk HR, Schultz AS, Richardson Jr JW. J Appl Phys 1997;71:594–600.
[16] Thompson SP, Parker JE, Potter J, Hill TP, Birt A, Cobb TM, et al. Rev Sci Instrum 2009:80.
[17] Christien F, Telling MTF, Knight KS. Scr Mater 2013;68:506–9.
[18] Takebayashi S, Kunieda T, Yoshinaga N, Ushioda K, Ogata S. Iron Steel Inst Jpn Int 2010;50:875–82.
[19] Rivera-Díaz-del-Castillo PEJ, Hayashi K, Galindo-Nava EI. Mater Sci Technol 2013;29:1206–11.
[20] Queyreau S, Monnet G, Devincre B. Acta Mater 2010;58:5586–95.
[21] San Martin D, Palizdar Y, Cochrane RC, Brydson R, Scott AJ. Mater Charact 2010;61:584–8.
[22] Chang LC, Bhadeshia HKDH. Mater Sci Technol 1995;11:874–81.
[23] Wang JS, Mulholland MD, Olson GB, Seidman DN. Acta Mater 2013;61:4939–52.
[24] Takeda K, Nakada N, Tsuchiyama T, Tataki S. Iron Steel Inst Jpn Int 2008;48:1122–5.
[25] Fribourg G, Brechét Y, Deschamps A, Simar A. Acta Mater 2011;59:3621–35.
[26] Proudhon H, Poole WJ, Wang X, Bréchet Y. Philos Mag 2008;88:621–40.
[27] Delincé M, Brechét Y, Embury JD, Geers MGD, Jacques PJ, Pardoen T. Acta Mater 2007;55:2337–50.
[28] Hull D, Bacon DJ. Introduction to dislocations. 5th ed. Butterworth Heinemann; 2011.
[29] Caron RN, Krauss G. Metall Trans 1972;3:2381–9.
[30] Brandon DG. Acta Metall 1966;14:1479–84.
[31] Winning M, Rollett AD. Acta Mater 2005;536:2901–7.
[32] Ghassemi-Armaki H, Chen RP, Maruyama K, Yoshizawa M, Igarashi M. Mater Lett 2009;63:2423–5.
[33] Wittig JE, Frommeyer G. Metall Mater Trans A 2008;39:252–65.